Journal Pre-proof

Sensitivity of near-infrared bands to cloud phase: An assessment using dual-view satellite measurements

Kameswara S. Vinjamuri, Marco Vountas, Vladimir Rozanov, Luca Lelli, Hartmut Boesch, John P. Burrows

PII: S0022-4073(26)00031-2
DOI: https://doi.org/10.1016/j.jqsrt.2026.109837
Reference: JQSRT 109837

To appear in: *Journal of Quantitative Spectroscopy and Radiative Transfer*

Received date : 19 June 2025
Revised date : 23 November 2025
Accepted date : 18 January 2026

Sensitivity of Near-Infrared Bands to Cloud Phase: An Assessment Using Dual-View Satellite Measurements

Kameswara S. Vinjamuri[a,*], Marco Vountas[a], Vladimir Rozanov[a], Luca Lelli[b], Hartmut Boesch[a], John P. Burrows[a]

[a]Institute of Environmental Physics, University of Bremen, Bremen, Germany
[b]Remote Sensing Technology Institute, German Aerospace Centre (DLR), Wessling, Germany

Abstract

Accurate cloud phase classification in the near-infrared is challenging due to the overlapping radiative properties of water, ice, and mixed-phase clouds. This study presents a new composite Phase Classification Index ($PCI_{NIR,DV}$) for near-infrared satellite measurements in a dual-viewing geometry. The index is defined as the product of two physically derived components: (1) a spectral ratio of top-of-atmosphere radiances at 1.61 µm and 2.25 µm, which exploits the differences in absorption between water and ice, and (2) a directional ratio of 0.87 µm radiances from oblique and nadir views, which are influenced by scattering. Theoretical simulations using the SCIATRAN radiative transfer model demonstrate that the $PCI_{NIR,DV}$ effectively distinguishes between pure water and ice clouds, enabling mixed-phase clouds to be identified. Sensitivities are analyzed for ranges of particle sizes, ice fractions, and surface types. Theoretical results show that water clouds, excluding thin clouds over snow surfaces, exhibit high $PCI_{NIR,DV}$ values (above 3.5), ice clouds yield low values (below 2.75), and intermediate values correspond to mixed-phase clouds. Validation of $PCI_{NIR,DV}$ derived from the Sea and Land Surface Temperature Radiometer (SLSTR) dual-view observations (onboard Sentinel-3A) against CloudSat-CALIPSO phase classifications confirms its applicability, yielding 86% classification accuracy, including over 63% for mixed-phase clouds. The results demonstrate that $PCI_{NIR,DV}$ provides a robust physical framework for dual-view satellite missions, which aim to measure the cloud phase.

Keywords:
Cloud phase, Mixed-phase clouds, SCIATRAN, Dual-view, Satellite remote

*Corresponding author
Email address: kamesh@iup.physik.uni-bremen.de (Kameswara S. Vinjamuri)

sensing

1. Introduction

The wavelength-dependent solar radiation leaving the cloudy atmosphere is strongly influenced by cloud physical properties, such as thermodynamic phase, optical thickness and particle size[1–3]. Accurate identification of the cloud phase is important for understanding how clouds influence Earth's radiation budget [4–6]. Phase identification is also an essential step for satellite-based cloud property retrievals [7–10]. Although many techniques exist for distinguishing between water and ice clouds in the solar wavelengths, they often have limitations in scenes with strong surface reflectance or optically thin clouds [2, 11]. In addition to pure-phase clouds such as water and ice, mixed-phase clouds (MPC) add more complexities because they contain both supercooled liquid droplets and ice crystals. This coexistence of water and ice makes radiance signals from MPC resemble those of pure-phase clouds, making accurate detection even more challenging [12, 13].

Various techniques have been developed to discriminate cloud thermodynamic phases using passive remote sensing instruments. Chylek et al. [14] utilized a simple band ratio approach involving radiances at 0.87 µm and 1.65 µm, measured by the Multispectral Imager, for separating cloud phases. Nagao et al. [13] use shortwave infrared observations from passive sensors to characterize cloud phase. Hyperspectral methods in the 1.40 – 1.80 µm range are explored by Thompson et al. [8], Knap et al. [15], Acarreta et al. [16], Kokhanovsky et al. [17], Ehrlich et al. [18], demonstrating the usefulness of high spectral resolution data for cloud phase classification. However, these approaches, which rely on single-view measurements for cloud phase classification, have limitations. This is because the satellite only measures photons from a single direction, and the classification of cloud phase typically relies on bands from this single-view, which raises the problem of spectral signature overlap between cloud phases. Since the scattering of non-spherical ice crystals differs from spherical water droplets as a function of the viewing direction, using combinations of viewing geometries provides additional and enhanced directional information, thereby improving cloud phase classification. MPC are particularly difficult to classify because of their occurrence with varying proportions of water and ice along with particle sizes [12, 19]. Despite their relevance, relatively few studies have examined which MPC occurrences are spectrally distinguishable in the solar NIR bands and under what conditions the MPC assignment becomes ambiguous [8, 14, 20].

This study investigates the sensitivity of cloud phase classification in the NIR spectral bands, which are commonly used for cloud remote sensing (0.87 µm, 1.61 µm, 2.25 µm) [21–26]. Section 2 describes the radiative transfer setup used in this study. This setup utilizes the radiative transfer software package SCIATRAN [27], which accurately simulates spectral and directional radiances for varying cloud microphysical properties and surface conditions. Section 3 discusses the intrinsic physical properties of water and ice, which are crucial for understanding whether absorption or scattering dominates in different parts of the spectrum. In Section 4, the sensitivity results of the spectral indexes are assessed for various ranges of cloud optical and microphysical properties. The best possible index, formulated using angular scattering sensitivity at 0.87 µm and spectral absorption differences at 1.61 µm and 2.25 µm, is tested for MPC to determine whether it can be distinguished from pure-phase clouds. To validate this index, dual-view measurements from the Sea and Land Surface Temperature Radiometer (SLSTR) onboard Sentinel-3A, co-located with cloud phase classifications from the CloudSat-CALIPSO product [28] are used (Section 5). Finally, Section 6 concludes the broader implications of these findings for operational remote sensing of the cloud phase, especially for dual-view satellite measurements.

Table 1: Input parameters for radiative transfer simulations using SCIATRAN

Phase	Ice, Mixed, Liquid
r_{eff} (liquid clouds)	4, 6, 8, 12, 16 μm
D_{max} (ice clouds)	45, 90, 135, 180 μm
τ (COD)	1, 3, 5, 10, 15, 20, 30, 50, 80
$\mathrm{IF}_{\mathrm{COD}}$	0, 0.2, 0.4, 0.6, 0.8, 1
CTH - CBH	2.5 km - 2 km
Gas absorption	Off
SZA	45°
Surface type	Ocean, Snow

2. Radiative Transfer Parametrization

SCIATRAN simulates radiances by solving the vector or scalar radiative transfer equation using the discrete ordinates method. This study employs a pseudo-spherical geometry for the solar beam to more accurately account for atmospheric curvature at high solar zenith angles. The diffuse radiation field is treated in a plane-parallel atmosphere. For unpolarized radiation, the radiance $I(\tau, \mu, \phi)$ as a function of optical depth τ, cosine of zenith angle μ, and azimuth angle ϕ satisfies the following integral-differential equation:

$$\begin{aligned}\mu \frac{dI(\tau,\mu,\phi)}{d\tau} = & - I(\tau,\mu,\phi) \\ & + \frac{\omega_0(\tau)}{4\pi} \int_{-1}^{1} \int_{0}^{2\pi} P(\mu,\phi;\mu',\phi') \cdot I(\tau,\mu',\phi')\, d\phi' d\mu' \\ & + S_{\text{sun}}^{\text{ps}}(\tau,\mu,\phi) \end{aligned} \tag{1}$$

where $\omega_0 = \beta_{\text{sca}}/\beta_{\text{ext}}$ is the single scattering albedo, $P(\mu, \phi; \mu', \phi')$ is phase function, and $S_{\text{sun}}^{\text{ps}}$ denotes the pseudo-spherical single scattering source term arising from the attenuated direct solar beam. The extinction coefficient $\beta_{\text{ext}}(\lambda)$ is defined by:

$$\beta_{\text{ext}}(\lambda) = \int \pi r^2\, Q_{\text{ext}}(r, \lambda; m(\lambda)) \cdot N(r)\, dr, \tag{2}$$

where Q_{ext} is the extinction efficiency, $N(r)$ is the particle size distribution, and $m(\lambda) = n(\lambda) + ik(\lambda)$ is the complex refractive index. In this work, the refractive index of pure water is taken from [29], whereas ice refractive index data followed [30]. The underlying surface's bidirectional reflectance (BRDF) is modeled using physically consistent BRDF models available in SCIATRAN [31]. For the ocean surface, the model includes Fresnel reflection and a modified Gordon approximation for water-leaving radiance [31, 32]. For the snow surface, an asymptotic radiative transfer model for granular media is used [33]. The cloud is assumed to be vertically homogeneous within the atmospheric column. As with most passive spectrometer-based studies, the results presented here primarily represent the effective properties at the cloud top. The size distribution of water droplets is assumed to follow a gamma distribution [31, 34]. The optical properties of water droplets are calculated using the Lorenz–Mie theory [35]. For nonspherical ice particles, the gamma distribution function is employed to represent the polydisperse nature of the particles. The optical properties of ice crystals are obtained from Yang's database [36], which provides precomputed values for various ice crystal habits at different maximal dimensions and wavelengths. Table 1 shows the effective radii (r_{eff}) for water clouds and maximal dimensions (D_{max}) for ice clouds that are considered in this study. Previous work has shown that the ice crystal shape and its roughness have far less impact compared to their effective size [12, 37]. Based on this, a moderately rough solid column habit for ice crystals is used in our simulations. Nevertheless, the results presented in Fig.2, i.e., scattering phase functions, remain representative and applicable for various crystal shapes (not shown here). For MPC, the extinction coefficient ($\beta_{\text{ext}}^{\text{mix}}$), single scattering albedo (ω_0^{mix}), and the phase function ($P^{\text{mix}}(\theta)$) are defined as:

$$\beta_{\text{ext}}^{\text{mix}} = f_w \beta_{\text{ext}}^{\text{water}} + f_i \beta_{\text{ext}}^{\text{ice}}, \quad \omega_0^{\text{mix}} = \frac{f_w \omega_0^{\text{water}} \beta_{\text{ext}}^{\text{water}} + f_i \omega_0^{\text{ice}} \beta_{\text{ext}}^{\text{ice}}}{\beta_{\text{ext}}^{\text{mix}}}, \tag{3}$$

$$P^{\text{mix}}(\theta) = \frac{f_w \beta_{\text{sca}}^{\text{water}} P^{\text{water}}(\theta) + f_i \beta_{\text{sca}}^{\text{ice}} P^{\text{ice}}(\theta)}{f_w \beta_{\text{sca}}^{\text{water}} + f_i \beta_{\text{sca}}^{\text{ice}}}, \tag{4}$$

where f_w and $f_i = 1 - f_w$ are the water and ice volume fractions, respectively, and $\beta_{\text{sca}} = \omega_0 \cdot \beta_{\text{ext}}$ for each phase. The angle θ in the above equation denotes the scattering angle. In terms of cloud optical thickness (COD), the ice fraction, denoted as IF_{cod}, is defined as the ratio of the extinction optical depth due to ice to the total COD.

$$\text{IF}_{\text{COD}} = \frac{\tau_{\text{ice}}}{\tau_{\text{ice}} + \tau_{\text{water}}}, \tag{5}$$

SCIATRAN simulations are performed for a comprehensive set of combinations as summarized in Table 1 to evaluate the radiative impact of different cloud phases.

3. Physical Basis

3.1. Intrinsic Properties

The refractive index, $m(\lambda)$, determines absorption and scattering radiative properties of water and ice, influencing both ω_0 and P in Eq. 1. Water

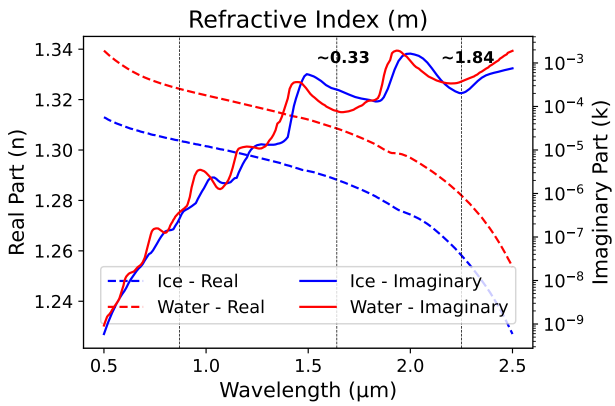

Figure 1: The plot shows the spectral variation of complex refractive index (real and imaginary parts) of water and ice (0.5–2.5 µm). The annotated values at 1.61 µm and 2.25 µm denote the water-to-ice ratio of the imaginary component (k) at those wavelengths. The vertical lines indicate the wavelengths used throughout the study.

and ice have wavelength-dependent $m(\lambda)$ as shown in Fig. 1 (the scattering and absorption coefficients of water and ice are presented in the appendix section: Fig. A.11). The $m(\lambda)$ of water and ice across the solar spectrum provides critical insights into their optical behavior when electromagnetic radiation interacts with them. The real part of the refractive index (n) for both water and ice decreases gradually with wavelength, indicating a decline in scattering efficiency at longer wavelengths. At 0.87 µm, high real component values as compared to imaginary parts indicate that scattering dominates relatively over absorption. This wavelength is particularly significant as water and ice exhibit minimal absorption (low imaginary component, k), leading to strong scattering-driven radiative effects. The imaginary component (k) governs absorption and becomes more prominent as the wavelength increases, particularly at 1.61 µm and 2.25 µm. As shown in Fig. 1, at 1.61 µm, the imaginary part of the refractive index of water is approximately 0.33 times that of ice. In contrast, at 2.25 µm, water's imaginary component is about 1.84 times that of ice, indicating stronger absorption by water. These wavelength-dependent real and imaginary components are crucial for distinguishing between the cloud phases, as will be shown in Section 4.

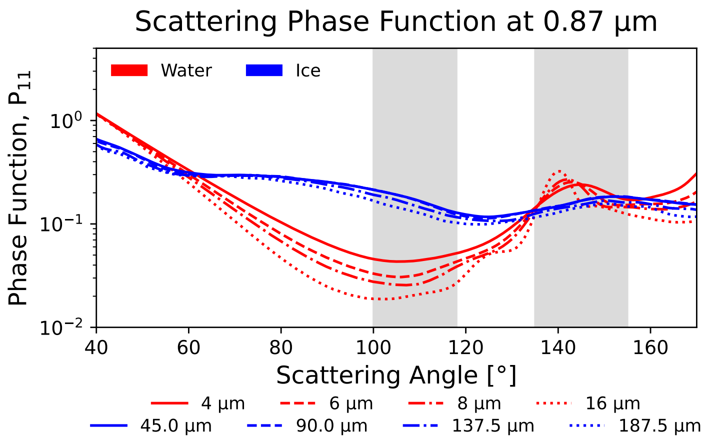

Figure 2: Phase function at 0.87 µm of ice (solid column) crystals and water droplets at different maximal dimensions and effective radii, respectively, for polydisperse distributions as described in Section 2. The shaded region represents the occurrence of SLSTR observations used for validation described in Section 5.1.

3.2. Phase function

Figure 2 presents the phase functions (P) at 0.87 µm for water droplets and ice crystals of varying sizes. These angular scattering distributions describe how polydisperse particles redirect incident light and contribute directly to the source function term in Eq.1. The choice of the wavelength 0.87 µm is motivated by its minimal absorption and scattering-dominated regime, as shown in Fig.1. The phase functions of water droplets at 0.87 µm (Fig. 2) are characterized by a pronounced minimum of scattered intensity between 110° and 130°. In contrast, ice crystals have higher scattering in this range of scattering angles due to side scattering caused by their non-spherical form. For scattering angles exceeding 130°, the similarity in scattering magnitudes between water and ice indicates comparable backscattering responses. The reduction in scattering between 110° and 130° becomes more pronounced as the water droplet size increases. In contrast, the enhanced side scattering observed for ice remains prominent across all maximal dimensions. These scattering distinctions form a critical physical basis for cloud phase differentiation. In particular, instruments with dual-view geometries, such as SLSTR, which can provide scattering angles between 100° and 120° and 135° and 150°, can exploit directional radiances to infer cloud phase.

4. Sensitivity results

4.1. Water and Ice phase clouds

As discussed in Section 3.1, the imaginary part of the refractive index governs the spectral absorption characteristics of cloud particles. At 1.61 µm, ice exhibits stronger absorption than water (due to the high imaginary part), resulting in lower top-of-atmosphere (TOA) radiances. Conversely, at 2.25 µm, absorption by water dominates. Also importantly, absorption at 1.61 µm and 2.25 µm increases with particle size [1, 38]. Since ice crystals are generally larger than liquid droplets, this further suppresses the 1.61 µm and 2.25 µm TOA radiance in ice clouds. To exploit this spectral and microphysical contrast, we define the Phase Classification Index in the Near-Infrared ($\mathrm{PCI_{NIR}}$) as the ratio of TOA radiances:

$$\mathrm{PCI_{NIR}} = \frac{L^{\mathrm{n}}_{1.61}}{L^{\mathrm{n}}_{2.25}}, \tag{6}$$

Higher $\mathrm{PCI_{NIR}}$ values indicate water clouds, arising from their comparatively elevated TOA radiances at 1.61 µm relative to ice clouds. In contrast, ice clouds exhibit stronger absorption at this wavelength, producing systematically lower $\mathrm{PCI_{NIR}}$ values. This is illustrated in Fig. 3a, which depicts the dependence of $\mathrm{PCI_{NIR}}$ on COD for water and ice clouds across a range of particle sizes above an oceanic surface. The index exhibits a monotonic increase with COD for water clouds. Ice clouds, by contrast, show consistently lower $\mathrm{PCI_{NIR}}$ values with less sensitivity to D_{max}. The contrast between the two phases becomes increasingly discernible as COD increases. For COD values exceeding 5, $\mathrm{PCI_{NIR}}$ asymptotically approaches values below 2.5 for ice clouds and exceeds 3.0 for water clouds. Optically thin ice clouds (COD $\leq$ 3) show high values from 2.5 to 3.0 above the ocean surface. For the snow surface conditions, a similar spectral contrast is observed in $\mathrm{PCI_{NIR}}$ (Fig. 4a), but the absolute values are subtly modulated at lower COD values due to enhanced surface reflectance. Optically very thin water clouds (COD $\leq$ 1) have typically $\mathrm{PCI_{NIR}}$ below 2.5 and are very similar to that of ice clouds. As the COD increases, COD $\geq$ 5, the water clouds above the snow surface also show high values above 3.0. Ice clouds consistently exhibit $\mathrm{PCI_{NIR}}$ values below 2.5. This distinct phase separation highlights the utility of $\mathrm{PCI_{NIR}}$ as a reliable discriminator of cloud phase under optically thick conditions. A threshold value of 3 for $\mathrm{PCI_{NIR}}$ effectively distinguishes between water and ice clouds, with values greater than 3 indicating water clouds and values less than 3 indicating ice clouds. The separation remains robust under a highly reflective surface, implying consistency for water and snow surfaces.

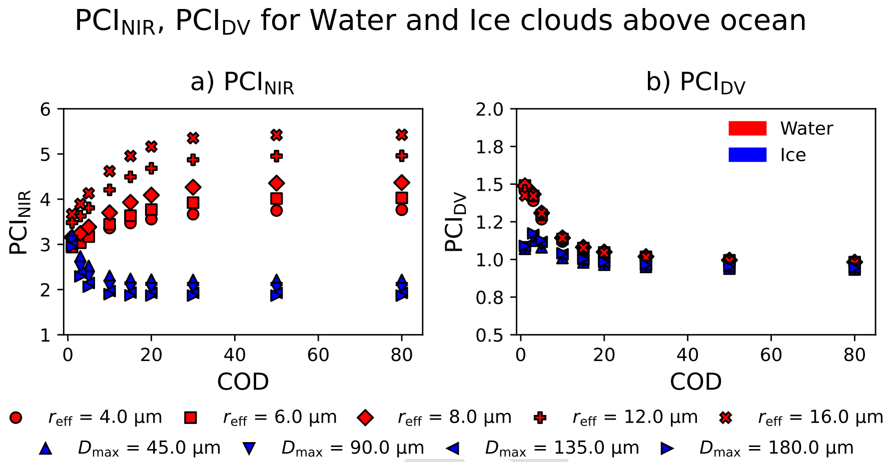

Figure 3: PCI$_{NIR}$, PCI$_{DV}$ for water and ice clouds over ocean surface.

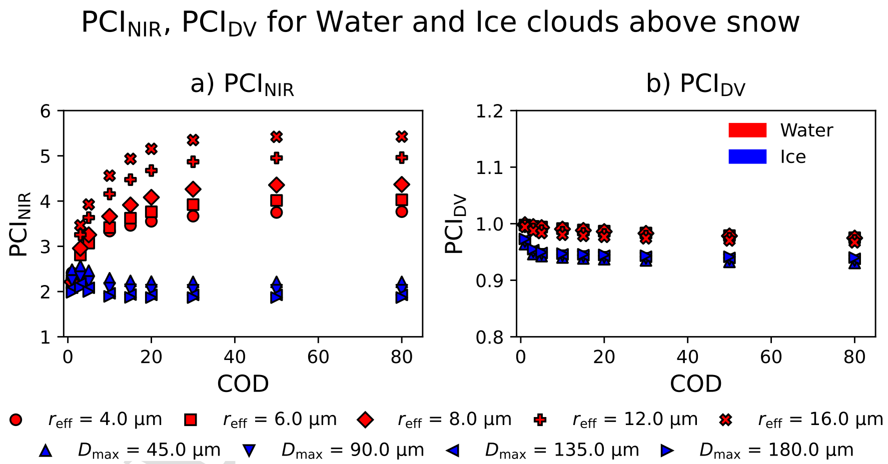

Figure 4: Same as Figure 3 over snow surface.

To quantitatively exploit the angular contrast in satellite observations, and to enhance the discrimination at low COD values, we define a Phase

Classification Index for Dual-View observations ($\mathrm{PCI_{DV}}$), as the ratio of radiance observed in an oblique-view geometry to that in a nadir-view geometry at 0.87 µm.

$$\mathrm{PCI_{DV}} = \frac{L^{\mathrm{o}}_{0.87}}{L^{\mathrm{n}}_{0.87}}, \tag{7}$$

This ratio emphasizes differences in the angular scattering signatures between water and ice clouds, providing a physical discriminator of cloud phase. A representative geometric configuration (oblique-view and nadir-view) observed by satellite is selected to assess the sensitivity of $\mathrm{PCI_{DV}}$. The oblique-view case corresponds to a scattering angle of approximately 134°, defined by a solar zenith angle (SZA) of 45°, a viewing zenith angle (VZA) of 55°, and a relative azimuth angle (RAA) of 120°. The nadir-view case corresponds to a scattering angle near 107° (SZA = 45°, VZA = 30°, RAA = 30°). Under these conditions, $\mathrm{PCI_{DV}}$ is computed as a function of COD, and the results are presented in Figure 3b (ocean surface) and Figure 4b (snow surface).

Above the ocean surface, for COD below 20, the $\mathrm{PCI_{DV}}$ for water clouds consistently exceeds that of ice clouds, regardless of r_{eff}. At lower COD values, COD ≤ 3, the $\mathrm{PCI_{DV}}$ of water clouds are 1.5 times that of ice clouds. As COD exceeds 20, multiple scattering becomes increasingly dominant, attenuating the directional radiance contrast. This attenuation reduces the discriminative capability of $\mathrm{PCI_{DV}}$. However, $\mathrm{PCI_{DV}}$ values for water clouds remain consistently higher than those for ice clouds across the COD range. In the presence of a snow surface (Figure 4), the $\mathrm{PCI_{DV}}$ values for optically thin clouds (COD ≤ 1) are less distinct for water and ice clouds, owing to the angular influence of the underlying snow surface. These findings demonstrate that radiances from different viewing angles, particularly at 0.87 µm where scattering dominates, are effective in identifying cloud phases even in optically thin to moderately thick layers.

Building upon the complementary sensitivities to enhance the discrimination between cloud phases, particularly in optically thin to moderately thick conditions, we introduce a composite phase classification index, $\mathrm{PCI_{NIR,DV}}$, defined as the product of $\mathrm{PCI_{NIR}}$ and $\mathrm{PCI_{DV}}$.

$$\mathrm{PCI_{NIR,DV}} = \mathrm{PCI_{NIR}} \times \mathrm{PCI_{DV}} = \left(\frac{L^{\mathrm{n}}_{1.61}}{L^{\mathrm{n}}_{2.25}}\right) \times \left(\frac{L^{\mathrm{o}}_{0.87}}{L^{\mathrm{n}}_{0.87}}\right) \tag{8}$$

This approach combines the phase-sensitive absorption features at 1.61 µm and 2.25 µm with scattering differences at 0.87 µm. Figure 5 and 6 show

$PCI_{NIR,DV}$ varies with COD above the ocean and snow surface. Over both the ocean and snow surfaces, $PCI_{NIR,DV}$ effectively separates water and ice cloud phases across a wide range of COD and r_{eff}/D_{max} values. Water clouds consistently exhibit higher $PCI_{NIR,DV}$ values typically above 3—regardless of surface type, with values exceeding 5 for droplet sizes larger than 12 µm and remaining above 3.5 even at COD $\leq$ 3. Over both the ocean and snow surfaces, from the above we conclude that $PCI_{NIR,DV}$ can be used to identify water and ice cloud phases across a wide range of COD and r_{eff}/D_{max} values. Water clouds generally exhibit higher $PCI_{NIR,DV}$ values, typically exceeding 3.5. Even at COD $\leq$ 3, water clouds often remain above 3.5 over ocean surfaces. However, optically thin water clouds may fall slightly below this threshold over snow surfaces. Ice clouds, in contrast, have consistently lower values, typically below 2.75, except for optically thin clouds above the ocean surface. The $PCI_{NIR,DV}$ can be used to more effectively separate the cloud phase than methods using only single views of the upwelling radiation. This dual-view index combines two physically based indices, PCI_{NIR} and PCI_{DV}, both of which are sensitive to the distinct optical properties of water and ice clouds. As these components tend to produce higher values for water clouds and lower values for ice clouds, their product ($PCI_{NIR} \times PCI_{DV}$) drives the two phases toward opposite ends of the index range, thereby enhancing phase discrimination.

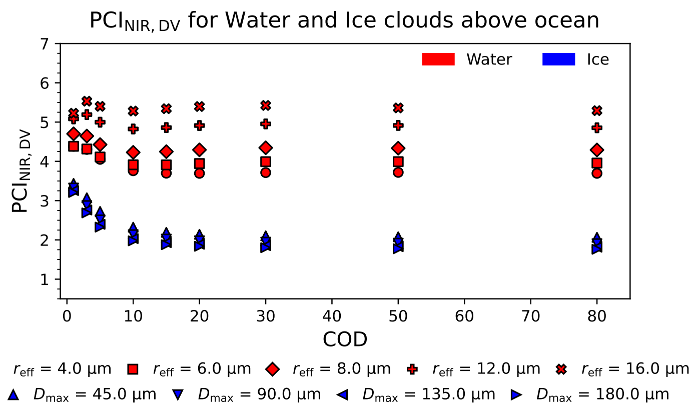

Figure 5: This plot shows the $PCI_{NIR,DV}$ for water and ice clouds over ocean surface. It is the combined index formed from PCI_{NIR} (3a) and PCI_{DV} (3b).

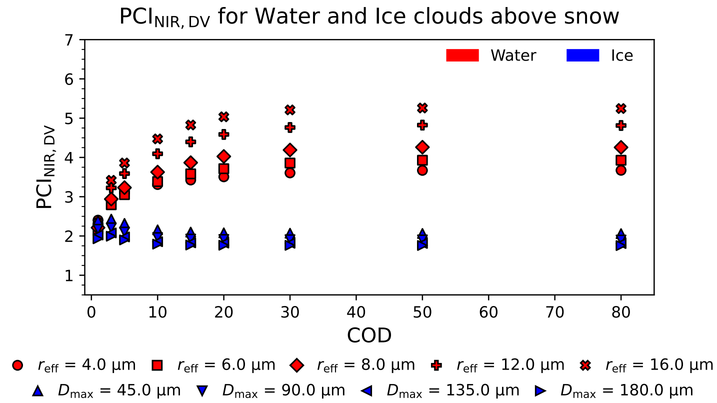

Figure 6: This plot shows the $\mathrm{PCI}_{\mathrm{NIR,DV}}$ for water and ice clouds over snow surface. It is the combined index formed from $\mathrm{PCI}_{\mathrm{NIR}}$ (4a) and $\mathrm{PCI}_{\mathrm{DV}}$ (4b).

4.2. MPC

As discussed above, the $\mathrm{PCI}_{\mathrm{NIR,DV}}$ values are higher for water clouds and lower for ice clouds, due to their contrasting spectral absorption and angular scattering properties. This separation defines an intermediate window to identify MPC, which exhibits liquid and ice optical characteristics (depending on their proportions). To evaluate $\mathrm{PCI}_{\mathrm{NIR,DV}}$ for MPC, we simulate a set of cloud configurations by varying COD, $\mathrm{IF}_{\mathrm{cod}}$, r_{eff}, D_{max} as summarized in Table 1. The results for MPC sensitivities above the ocean and snow surfaces are given in Figure 7 and Figure 8, respectively. These figures show the variation of the $\mathrm{PCI}_{\mathrm{NIR,DV}}$ for MPC, arranged in a 5-row by 4-column grid. Each row corresponds to a specific $\mathrm{IF}_{\mathrm{cod}}$, increasing from top to bottom: 0.2, 0.4, 0.5, 0.6, and 0.8. Each column represents a different D_{max} in the MPC for that corresponding $\mathrm{IF}_{\mathrm{cod}}$. Each subplot, indicates the variation of $\mathrm{PCI}_{\mathrm{NIR,DV}}$ with COD, as a function of r_{eff} for the MPC configuration. The shaded bands in each plot represent the ranges of $\mathrm{PCI}_{\mathrm{NIR,DV}}$ for pure water ($\mathrm{IF}_{\mathrm{cod}}$=0) and pure ice clouds ($\mathrm{IF}_{\mathrm{cod}}$=1), providing reference boundaries. The figure captures how the $\mathrm{PCI}_{\mathrm{NIR,DV}}$ changes for different combinations of COD, $\mathrm{IF}_{\mathrm{cod}}$, r_{eff}, D_{max}, revealing the conditions under which MPC signals overlap or can be separated from pure-phase clouds.

For MPC with an $\mathrm{IF}_{\mathrm{cod}} = 0.2$, i.e. low ice fractions (Figure 7a-d) above ocean, $\mathrm{PCI}_{\mathrm{NIR,DV}}$ exceeds 4 for optical thin clouds (COD ≤ 3). In this regime,

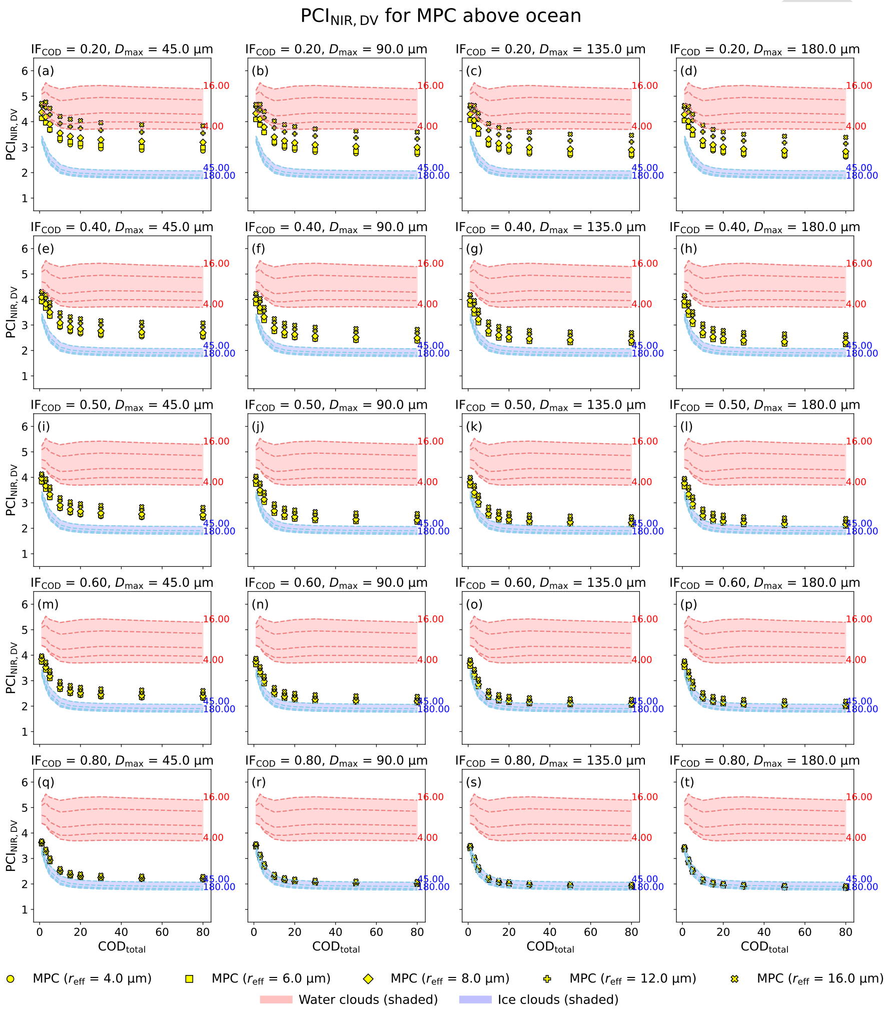

Figure 7: Plots of $\mathrm{PCI}_{\mathrm{NIR,DV}}$ as a function of COD for MPC over ocean. Rows correspond to increasing $\mathrm{IF}_{\mathrm{cod}}$, and columns represent increasing $D_{\max}$ in the MPC. Green points show MPC simulations for different r_{eff}. Shaded regions indicate the $\mathrm{PCI}_{\mathrm{NIR,DV}}$ ranges for water and ice clouds, allowing for a visual comparison with MPC cases.

the radiative signature closely resembles that from pure water clouds. As COD exceeds 10, $\mathrm{PCI}_{\mathrm{NIR,DV}}$ for MPC gradually decreases and typically falls

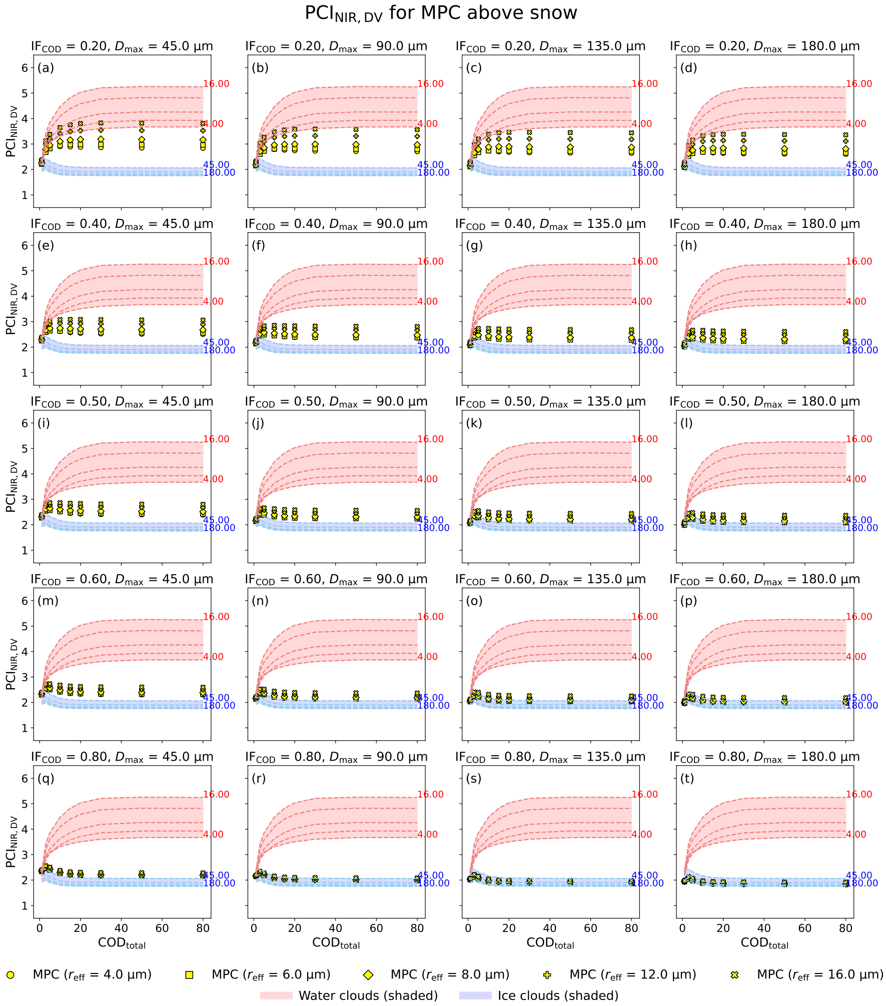

Figure 8: Same as Figure 7 for MPC over snow surface.

within the intermediate range of 2.75 to 3.5, where spectral signatures begin to separate from pure water. MPC containing large water droplets, particularly when the effective radius r_{eff} exceeds 12 µm, can still resemble pure water phase signatures when the ice fraction is low. The PCI$_{\text{NIR,DV}}$ values decrease with increasing $D_{\max}$, because larger ice crystals increase the extinction, due to the absorption at 1.61 µm and 2.25 µm. Overall, for low ice fractions $\mathrm{IF_{cod}} = 0.2$, when the MPC $D_{\max} \leq 45$ µm and $r_{\mathrm{eff}} \geq 12$ µm remain largely indistinguishable from pure water phase clouds. For intermediate ice fractions ($\mathrm{IF_{cod}} = 0.4$, 0.5, and 0.6), (Figure 7e-p), $\mathrm{PCI_{NIR,DV}}$ is consistently different from the pure water cloud regimes across all r_{eff} values. Optically thin MPC (COD ≤ 3) have values above 3.5 for intermediate ice fractions, making their $\mathrm{PCI_{NIR,DV}}$ less easily distinguishable from those of pure water clouds. As COD increases at this ice fraction, the $\mathrm{PCI_{NIR,DV}}$ values fall within the interval 2.5–3.75, gradually separating from both pure-phase signatures. For $\mathrm{IF_{cod}} = 0.6$, the $\mathrm{PCI_{NIR,DV}}$ decreases further, and the shift toward ice-like behavior becomes more pronounced. This ice-like behavior is more pronounced for MPC having $D_{\max} \geq 135$ µm. As the $\mathrm{IF_{cod}}$ reaches 0.6, the influence of r_{eff} within the MPC diminishes (Figure 7m-t). For MPC with a high ice fraction ($\mathrm{IF_{cod}} = 0.8$, Figure 7q-t), the $\mathrm{PCI_{NIR,DV}}$ is primarily governed by the radiative characteristics of the ice component. Across most combinations of particle sizes, the $\mathrm{PCI_{NIR,DV}}$ values fall below 2.75, approaching the range typical of ice clouds. When ice crystals are large ($D_{\max} \geq 135$ µm), the index fully overlaps with the ice regime across all COD levels, showing strong ice-phase features. Overall, for $\mathrm{IF_{cod}} = 0.8$, the $\mathrm{PCI_{NIR,DV}}$ strongly reflects ice-phase optical behavior, with phase discrimination becoming challenging. Over snow surfaces (Figure 8), the $\mathrm{PCI_{NIR,DV}}$ values for MPC exhibit similar trends to those observed over the ocean but with subtle surface-induced modulation for optically thin clouds (COD ≤ 3). At low ice fractions ($\mathrm{IF_{cod}} = 0.2$), MPC with high r_{eff} (≥ 12 µm) and low $D_{\max}$ (≤ 90 µm) still exhibit characteristics that overlap with those of pure water clouds. Unlike over the oceanic surface, the $\mathrm{PCI_{NIR,DV}}$ values for the optically thin MPC (COD ≤ 3) for $\mathrm{IF_{cod}} \geq 0.6$ are less than 2.5 due to enhanced surface effects. Optically very thin MPC (COD ≤ 1) above the ice (water) surface are hard to discriminate from pure ice (water) clouds using NIR bands.

To summarize, over ocean and snow surfaces, MPC with COD ≥ 3, and moderate ice fractions ($\mathrm{IF_{cod}} = 0.2 - 0.5$), exhibit $\mathrm{PCI_{NIR,DV}}$ values in the intermediate range 2.75 to 3.50. When ($\mathrm{IF_{cod}} = 0.6$) the $D_{\max}$ becomes a dominant factor, as $D_{\max}$ approaches 90 µm and beyond, $\mathrm{PCI_{NIR,DV}}$ values drop below the intermediate range. For MPCs with high ice fractions (0.8), distinguishing them from pure ice clouds over ocean and snow surfaces becomes increasingly difficult.

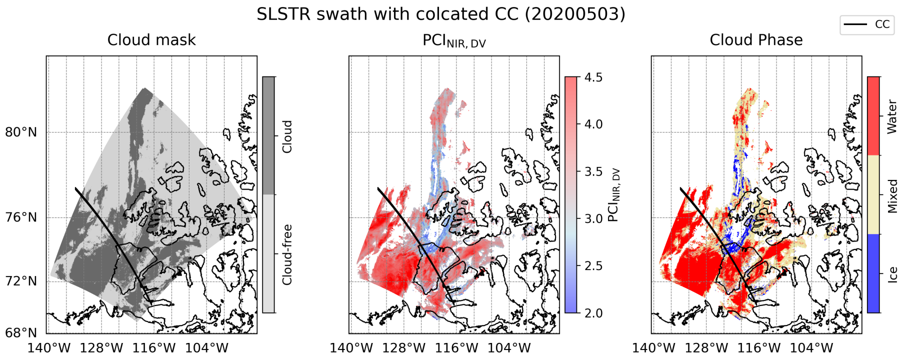

Figure 9: SLSTR cloud mask, $\mathrm{PCI}_{\mathrm{NIR,DV}}$ and cloud phase (classified as ice for $\mathrm{PCI}_{\mathrm{NIR,DV}}$ values below 2.75, above 3.5 as water, and in between as MPC) collocated with 2B-CLDCLASS-LIDAR product, CC (black line) for one swath on 2020-05-03.

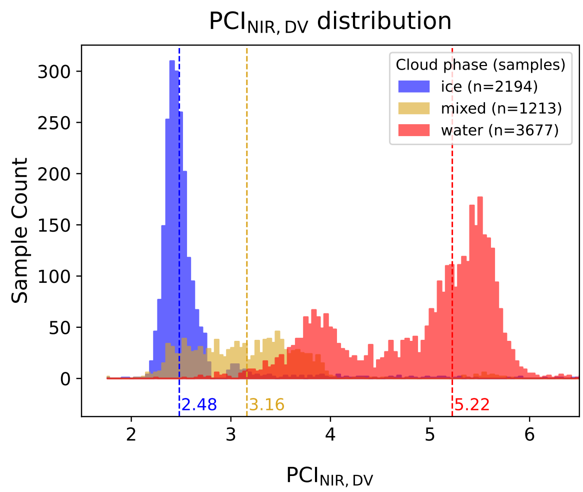

Figure 10: SLSTR $\mathrm{PCI}_{\mathrm{NIR,DV}}$ matched with cloud phase classification from CloudSat-Calipso for 2020-05-03

5. Validation

5.1. Data used

To validate the $\mathrm{PCI}_{\mathrm{NIR,DV}}$ for a dual-view spaceborne sensor, SLSTR data onboard the Sentinel-3A satellite are used for 3rd May 2020 [39]. The validation focuses on higher latitudes (above 60°N), where all cloud thermodynamic phases, including MPC, are frequent. The $PCI_{NIR,DV}$ is calculated using SLSTR L1B radiance data. SLSTR operates in dual-view mode, with nadir and oblique observations (viewing angles of 55°). The data used here are 500-meter NIR radiances at 0.87 µm, 1.61 µm, and 2.25 µm. In SLSTR dual-view observations, both viewing geometries are aligned at the surface level. Due to this, clouds exhibit a shift in the along-track direction between both views (parallax effect). To ensure that the dual-view observations correspond to the same cloud target, a parallax correction based on spatial correlation as described in [40] is applied. Once the parallax is corrected, $PCI_{NIR,DV}$ values are computed using the dual-view radiances from SLSTR. To evaluate this index, we validate it with the 2B-CLDCLASS-LIDAR product (CC), a merged dataset derived from the radar measurements of Cloud Profiling Radar (CPR) (on-board CloudSat) and lidar measurements Cloud-Aerosol Lidar with Orthogonal Polarization (CALIOP) (on-board CALIPSO) [41]. This synergistic product classifies the cloud thermodynamic phase (ice, liquid, or MPC) based on unique backscattering signatures from CALIOP and radar reflectivity from the CPR for up to 10 vertical cloud layers. Within this dataset, mixed-phase classification is assigned to cloud layers where lidar indicates the presence of liquid water and radar returns exhibit strong reflectivity. This combination suggests that supercooled droplets and ice particles coexist simultaneously. To avoid misclassification, we exclude scenes where a thin ice layer lies above water or MPC, since the goal is to identify the dominant phase within each matched vertical column.

In this analysis, the SLSTR $PCI_{NIR,DV}$ values and the CC product are collocated within a spatial threshold of 1 km and a temporal window of 5-minute intervals. The cloud mask is generated using the cloud flags available in the SLSTR Level-1B data. However, visual inspection revealed that snow surfaces are frequently misclassified as clouds. An additional screening criterion using Normalized Difference Snow Index (NDSI) is applied to address this (NDSI is calculated using 0.87 µm, 1.61 µm bands). The pixels with NDSI greater than 0.6 are excluded [42]. Figure 9 shows the SLSTR cloud mask and the $PCI_{NIR,DV}$ collocated with CC for one swath on 3rd May 2020. Only SLSTR pixels identified as cloudy and collocated with CC pixels having a cloud fraction greater than 0.8 are included in the comparison to ensure consistent cloud coverage. The scattering angles associated with the SLSTR dual-view geometry range from 100° to 120° in the nadir-view and 135° to 150° in the oblique-view, as shown in Figure 2.

Table 2: Confusion matrix (percentage) for cloud phase classification from SLSTR as compared to the merged dataset CloudSat and CALIOP (CC). The diagonal values represent correctly classified samples, while off-diagonal values indicate misclassifications.

Phase	Total Samples	Ice (%)	Mixed (%)	Water (%)
Ice	2194	87.24%	8.61%	4.15%
Mixed	1213	23.33%	63.73%	12.94%
Water	3677	0.08%	8.19%	91.73%
Overall Accuracy (%)		86%		

5.2. Validation Results

Figure 10 shows the distribution of $\mathrm{PCI}_{\mathrm{NIR,DV}}$ values calculated using SLSTR radiances for all swaths on 3rd May 2020, color-coded from cloud phases from collocated CC. Based on this distribution and from the theoretical sensitivity results, thresholds are selected to categorize the cloud types for the confusion matrix. The values below 2.75 are classified as ice, values above 3.5 as water, and values between these as MPC. Table 2 shows the confusion matrix, highlighting the percentage of correctly and incorrectly classified samples. The diagonal entries show the correct classifications, with ice clouds correctly identified in 87.24% of cases and water clouds in 91.73%. MPC, which are inherently more difficult to classify due to their spectral overlap with pure water and ice, are successfully identified in 63.73% of cases. While some misclassification occurred, with 23.33% of MPC being misidentified as ice and 12.94% as water, the ability to classify a significant fraction of MPC distinctly demonstrates the discriminatory power of $\mathrm{PCI}_{\mathrm{NIR,DV}}$. The biases may also arise from thresholding, as the cloud phase exhibits a continuous spectral gradient rather than a discrete classification. The overall classification accuracy of 86% further shows the effectiveness of this dual-view approach. For MPC, the accuracy is relatively lower compared to pure-phase clouds. However, their distinct spectral signatures suggest that they can be detected and monitored in the atmosphere.

6. Summary

Cloud phase identification in the near-infrared spectrum is challenging due to the overlapping absorption and varying scattering behaviors of water, ice, and mixed-phase clouds. Variations in surface reflectance due to different surfaces further intensify these challenges. This study proposes a physically based index using the $\mathrm{PCI}_{\mathrm{NIR,DV}}$, defined as the product of two complementary quantities:

- $\mathrm{PCI}_{\mathrm{NIR}}$, the spectral ratio of top-of-atmosphere radiances at 1.61 µm and 2.25 µm. This ratio exploits the difference in the absorption of water and ice clouds, having higher values for water clouds and lower values for ice clouds.

- $\mathrm{PCI}_{\mathrm{DV}}$, the ratio of radiances at 0.87 µm from oblique and nadir views, which exploits angular scattering differences between water and ice. This ratio is also higher for water clouds and lower for ice clouds.

$\mathrm{PCI}_{\mathrm{NIR}}$ and $\mathrm{PCI}_{\mathrm{DV}}$ are simultaneously high for water clouds and low for ice clouds, reflecting their physical dependence on absorption and scattering properties. As a result, their product, $\mathrm{PCI}_{\mathrm{NIR,DV}}$, extends the dynamic range of the index and enhances phase separation. This separation pushes pure-phase clouds toward opposite ends of the index space. It creates a physically intermediate region where clouds with mixed-phase characteristics fall, depending on their ice fraction, particle sizes, and cloud optical thickness. Radiative transfer simulations using SCIATRAN show the effectiveness and limitations of $\mathrm{PCI}_{\mathrm{NIR,DV}}$. To validate this index, $\mathrm{PCI}_{\mathrm{NIR,DV}}$ calculated from dual-view SLSTR observations are collocated with the cloud phase information from CloudSat-CALIPSO. The validation results confirm the applicability of $\mathrm{PCI}_{\mathrm{NIR,DV}}$ for cloud phase classification for the dual-view satellite measurements. Overall, the method achieved an accuracy of 86%, with water and ice clouds correctly classified in more than 87% of cases. For MPC, the accuracy was over 63%. These results suggest that the dual-view setup helps improve cloud phase detection, especially for complex MPC cases. The $\mathrm{PCI}_{\mathrm{NIR,DV}}$ framework provides a physically consistent and adaptable approach for the current and next-generation satellite missions with multi-angle observation capabilities.

Appendix A. Scattering and absorption coefficients

The plot below shows the scattering and absorption coefficients of water and ice

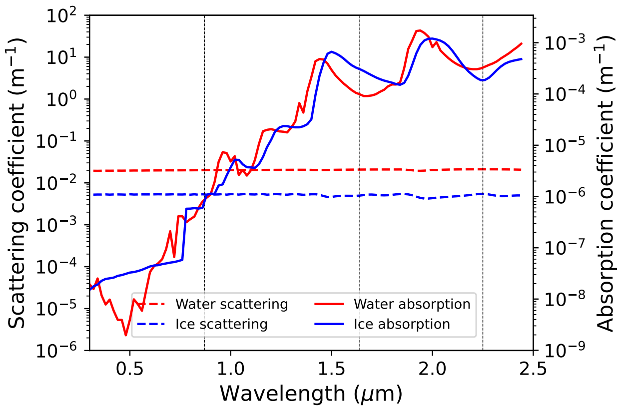

Figure A.11: The plot shows the Spectral variation of absorption and scattering coefficients of water ($r_{\text{eff}} = 8$ µm) and ice ($D_{\text{max}} = 90$ µm) for $0.1\,\text{g/m}^3$. The vertical lines indicate the wavelengths used in this study.

Data availability

SCIATRAN is available for access from the Institute of Environmental Physics (IUP) (https://www.iup.uni-bremen.de/sciatran/). Contains modified Copernicus Sentinel data [2020]. The SLSTR L1B data can be accessed from the Copernicus Data Space Ecosystem (CDSE) https://browser.dataspace.copernicus.eu/. The 2B-CLDCLASS-LIDAR data can be accessed at https://www.cloudsat.cira.colostate.edu/data-products/2b-cldclass-lidar; last access: February 2024.

Declaration of competing interest

The authors declare they have no competing interests.

Acknowledgments

We gratefully acknowledge the European Space Agency (ESA) for the Sentinel-3 mission, and especially thank the SLSTR team. Acknowledgments to NASA for the CloudSat and CALIPSO missions. Acknowledgments to the CloudSat Data Processing Center for providing the 2B-CLDCLASS-LIDAR data. We acknowledge the University of Bremen for its support and funding of this research. We gratefully acknowledge the funding by the Deutsche Forschungsgemeinschaft (DFG, German Research Foundation) – project no. 268020496 – TRR 172, within the Transregional Collaborative Research Center "ArctiC Amplification: Climate Relevant Atmospheric and SurfaCe Processes, and Feedback Mechanisms $(AC)^3$". This work is made possible by the use of a high-performance computing (HPC) system. We would like to thank the DFG for providing the HPC system Hypatia, which was funded under the grant GZ INST 144/493-1 FUGG.

References

[1] T. Nakajima, M. D. King, Determination of the optical thickness and effective particle radius of clouds from reflected solar radiation measurements, Journal of the Atmospheric Sciences 47 (15) (1990) 1878–1893. doi:10.1175/1520-0469(1990)047<1878:DOTOTA>2.0.CO;2.

[2] S. Platnick, M. King, S. Ackerman, W. Menzel, B. Baum, J. Riedi, R. Frey, The modis cloud products: algorithms and examples from terra, IEEE Transactions on Geoscience and Remote Sensing 41 (2) (2003) 459–473. doi:10.1109/TGRS.2002.808301.

[3] H. Letu, K. Yang, T. Y. Nakajima, H. Ishimoto, T. M. Nagao, J. Riedi, A. J. Baran, R. Ma, T. Wang, H. Shang, P. Khatri, L. Chen, C. Shi, J. Shi, High-resolution retrieval of cloud microphysical properties and surface solar radiation using himawari-8/ahi next-generation geostationary satellite, Remote Sensing of Environment 239 (2020) 111583. doi:10.1016/j.rse.2019.111583.

[4] G. L. Stephens, D. G. Vane, R. J. Boain, G. G. Mace, K. Sassen, Z. Wang, A. J. Illingworth, E. J. O'Connor, W. B. Rossow, S. L. Durden, The cloudsat mission and the a-train: A new dimension of space-based observations of clouds and precipitation, Bulletin of the American Meteorological Society 83 (12) (2002) 1771–1790. doi:10.1175/BAMS-83-12-1771.

[5] A. Bodas-Salcedo, P. G. Hill, K. Furtado, K. D. Williams, P. R. Field, J. Manners, P. Hyder, S. Kato, Large contribution of supercooled liquid clouds to the solar radiation budget of the southern ocean, Journal of Climate 29 (11) (2016) 4213–4228. doi:10.1175/JCLI-D-15-0564.1.

[6] L. Lelli, M. Vountas, N. Khosravi, J. P. Burrows, Satellite remote sensing of regional and seasonal arctic cooling showing a multi-decadal trend towards brighter and more liquid clouds, Atmospheric Chemistry and Physics 23 (4) (2023) 2579–2611. doi:10.5194/acp-23-2579-2023.

[7] J. Lee, P. Yang, A. Dessler, B. Baum, S. Platnick, The influence of thermodynamic phase on the retrieval of mixed-phase cloud microphysical and optical properties in the visible and near-infrared region, IEEE Geoscience and Remote Sensing Letters 3 (3) (2006) 287–291. doi:10.1109/LGRS.2006.864374.

[8] D. R. Thompson, I. McCubbin, B. C. Gao, R. O. Green, A. A. Matthews, F. Mei, K. G. Meyer, S. Platnick, B. Schmid, J. Tomlinson, E. Wilcox, Measuring cloud thermodynamic phase with shortwave infrared imaging spectroscopy, Journal of Geophysical Research: Atmospheres 121 (15) (2016) 9174–9190. doi:10.1002/2016JD024999.

[9] G. G. Wind, S. Platnick, K. Meyer, T. Arnold, N. Amarasinghe, B. Marchant, C. Wang, The chimaera system for retrievals of cloud top, optical and microphysical properties from imaging sensors, Computers & Geosciences 134 (2020) 104345. doi:10.1016/j.cageo.2019.104345.

[10] Y. Li, B. A. Baum, A. K. Heidinger, W. P. Menzel, E. Weisz, Improvement in cloud retrievals from viirs through the use of infrared absorption channels constructed from viirs+cris data fusion, Atmospheric Measurement Techniques 13 (7) (2020) 4035–4049. doi:10.5194/amt-13-4035-2020.

[11] J. Riedi, B. Marchant, S. Platnick, B. A. Baum, F. Thieuleux, C. Oudard, F. Parol, J.-M. Nicolas, P. Dubuisson, Cloud thermodynamic phase inferred from merged polder and modis data, Atmospheric Chemistry and Physics 10 (23) (2010) 11851–11865. doi:10.5194/acp-10-11851-2010.

[12] E. Ruiz-Donoso, A. Ehrlich, M. Schäfer, E. Jäkel, V. Schemann, S. Crewell, M. Mech, B. S. Kulla, L.-L. Kliesch, R. Neuber, M. Wendisch, Small-scale structure of thermodynamic phase in arctic mixed-phase clouds observed by airborne remote sensing during a cold air outbreak and a warm air advection event, Atmospheric Chemistry and Physics 20 (9) (2020) 5487–5511. doi:10.5194/acp-20-5487-2020.

[13] T. M. Nagao, K. Suzuki, Temperature-independent cloud phase retrieval from shortwave-infrared measurement of gcom-c/sgli with comparison to calipso, Earth and Space Science 8 (11) (2021) e2021EA001912. doi:10.1029/2021EA001912.

[14] P. Chylek, C. Borel, Mixed phase cloud water/ice structure from high spatial resolution satellite data, Geophysical Research Letters 31 (14) (2004). doi:10.1029/2004GL020428.

[15] W. H. Knap, P. Stammes, R. B. A. Koelemeijer, Cloud thermodynamic-phase determination from near-infrared spectra of reflected sunlight, Journal of the Atmospheric Sciences 59 (1) (2002) 83 – 96. doi:10.1175/1520-0469(2002)059<0083:CTPDFN>2.0.CO;2.

[16] J. Acarreta, P. Stammes, W. Knap, First retrieval of cloud phase from sciamachy spectra around 1.6 µm, Atmospheric Research 72 (1) (2004) 89–105, clouds and Radiation. doi:10.1016/j.atmosres.2004.03.027.

[17] A. Kokhanovsky, O. Jourdan, J. Burrows, The cloud phase discrimination from a satellite, Geoscience and Remote Sensing Letters, IEEE 3 (2006) 103 – 106. doi:10.1109/LGRS.2005.858487.

[18] A. Ehrlich, E. Bierwirth, M. Wendisch, J.-F. Gayet, G. Mioche, A. Lampert, J. Heintzenberg, Cloud phase identification of arctic boundary-layer clouds from airborne spectral reflection measurements: test of three approaches, Atmospheric Chemistry and Physics 8 (24) (2008) 7493–7505. doi:10.5194/acp-8-7493-2008.

[19] M. D. Shupe, S. Y. Matrosov, T. Uttal, Arctic mixed-phase cloud properties derived from surface-based sensors at sheba, Journal of the Atmospheric Sciences 63 (2) (2006) 697 – 711. doi:10.1175/JAS3659.1.

[20] S. D. Miller, Y.-J. Noh, A. K. Heidinger, Liquid-top mixed-phase cloud detection from shortwave-infrared satellite radiometer observations: A physical basis, Journal of Geophysical Research: Atmospheres 119 (13) (2014) 8245–8267. doi:10.1002/2013JD021262.

[21] C. Carbajal Henken, Satellite cloud property retrievals for climate studies using synergistic aatsr and meris measurements, Ph.D. thesis, Freie

Universität Berlin (2015).
URL https://refubium.fu-berlin.de/handle/fub188/12011

[22] B. Marchant, S. Platnick, K. Meyer, G. T. Arnold, J. Riedi, Modis collection 6 shortwave-derived cloud phase classification algorithm and comparisons with caliop, Atmospheric Measurement Techniques 9 (4) (2016) 1587–1599. doi:10.5194/amt-9-1587-2016.

[23] M. Stengel, S. Stapelberg, O. Sus, C. Schlundt, C. Poulsen, G. Thomas, M. Christensen, C. Carbajal Henken, R. Preusker, J. Fischer, A. Devasthale, U. Willén, K.-G. Karlsson, G. R. McGarragh, S. Proud, A. C. Povey, R. G. Grainger, J. F. Meirink, A. Feofilov, R. Bennartz, J. S. Bojanowski, R. Hollmann, Cloud property datasets retrieved from avhrr, modis, aatsr and meris in the framework of the cloud_cci project, Earth System Science Data 9 (2) (2017) 881–904. doi:10.5194/essd-9-881-2017.

[24] S. Platnick, K. G. Meyer, M. D. King, G. Wind, N. Amarasinghe, B. Marchant, G. T. Arnold, Z. Zhang, P. A. Hubanks, R. E. Holz, P. Yang, W. L. Ridgway, J. Riedi, The modis cloud optical and microphysical products: Collection 6 updates and examples from terra and aqua, IEEE Transactions on Geoscience and Remote Sensing 55 (1) (2017) 502–525. doi:10.1109/TGRS.2016.2610522.

[25] M. J. Tauc, D. W. Riesland, L. M. Eshelman, W. Nakagawa, J. A. Shaw, Simulations and experimental results of cloud thermodynamic phase classification with three SWIR spectral bands, Journal of Applied Remote Sensing 13 (3) (2019) 034526. doi:10.1117/1.JRS.13.034526.

[26] K.-G. Karlsson, M. Stengel, J. F. Meirink, A. Riihelä, J. Trentmann, T. Akkermans, D. Stein, A. Devasthale, S. Eliasson, E. Johansson, N. Håkansson, I. Solodovnik, N. Benas, N. Clerbaux, N. Selbach, M. Schröder, R. Hollmann, Clara-a3: The third edition of the avhrr-based cm saf climate data record on clouds, radiation and surface albedo covering the period 1979 to 2023, Earth System Science Data 15 (11) (2023) 4901–4926. doi:10.5194/essd-15-4901-2023.

[27] V. Rozanov, A. Rozanov, A. Kokhanovsky, J. Burrows, Radiative transfer through terrestrial atmosphere and ocean: Software package sciatran,

Journal of Quantitative Spectroscopy and Radiative Transfer 133 (2014) 13–71. doi:10.1016/j.jqsrt.2013.07.004.

[28] Z. Wang, CloudSat 2B-CLDCLASS-LIDAR product process description and interface control document, computer software manual (2019). URL https://www.cloudsat.cira.colostate.edu/cloudsat-static/info/dl/2b-cldclass-lidar/2B-CLDCLASS-LIDAR_PDICD.P1_R05.rev0_.pdf

[29] D. J. Segelstein, The complex refractive index of water, Ph.D. thesis, University of Missouri–Kansas City (1981).

[30] S. G. Warren, R. E. Brandt, Optical constants of ice from the ultraviolet to the microwave: A revised compilation, Journal of Geophysical Research: Atmospheres 113 (D14) (2008). doi:10.1029/2007JD009744.

[31] L. Mei, V. Rozanov, A. Rozanov, J. P. Burrows, Sciatran software package (v4.6): update and further development of aerosol, clouds, surface reflectance databases and models, Geoscientific Model Development 16 (5) (2023) 1511–1536. doi:10.5194/gmd-16-1511-2023.

[32] E. C. Monahan, I. G. O. Muircheartaigh, Optimal power-law description of oceanic whitecap coverage dependence on wind speed, Journal of Physical Oceanography 10 (1980) 2094–2099. doi:10.1175/1520-0485(1980)010<2094:OPLDOO>2.0.CO;2.

[33] A. A. Kokhanovsky, E. P. Zege, Scattering optics of snow, Appl. Opt. 43 (7) (2004) 1589–1602. doi:10.1364/AO.43.001589.

[34] A. A. Kokhanovsky, Cloud optics, Vol. 283, Springer, 2006. doi:10.1007/1-4020-4020-2.

[35] M. I. Mishchenko, J. M. Dlugach, E. G. Yanovitskij, N. T. Zakharova, Bidirectional reflectance of flat, optically thick particulate layers: an efficient radiative transfer solution and applications to snow and soil surfaces, Journal of Quantitative Spectroscopy and Radiative Transfer 63 (2) (1999) 409–432. doi:10.1016/S0022-4073(99)00028-X.

[36] P. Yang, L. Bi, B. Baum, K.-N. Liou, G. Kattawar, B. Cole, Spectrally consistent scattering, absorption, and polarization properties of atmospheric ice crystals at wavelengths from 0.2 to 100 µm, Journal of Atmospheric Sciences 70 (2013) 330–347. doi:10.1175/JAS-D-12-039.1.

[37] L. Forster, B. Mayer, Ice crystal characterization in cirrus clouds iii: retrieval of ice crystal shape and roughness from observations of halo displays, Atmospheric Chemistry and Physics 22 (23) (2022) 15179–15205. doi:10.5194/acp-22-15179-2022.

[38] M. D. King, S.-C. Tsay, S. E. Platnick, M. Wang, K.-N. Liou, Cloud retrieval algorithms for modis: Optical thickness, effective particle radius, and thermodynamic phase, MODIS Algorithm Theoretical Basis Document 1997 (1997) 440.
URL https://www.patarnott.com/satsens/pdf/atbd_mod05.pdf

[39] Copernicus Sentinel-3, SLSTR level-1b product SL_1_RBT [dataset], https://documentation.dataspace.copernicus.eu/Data/SentinelMissions/Sentinel3.html#sentinel-3-slstr-level-1, european Space Agency (2016).

[40] T. H. Virtanen, P. Kolmonen, E. Rodríguez, L. Sogacheva, A.-M. Sundström, G. de Leeuw, Ash plume top height estimation using aatsr, Atmospheric Measurement Techniques 7 (8) (2014) 2437–2456. doi:10.5194/amt-7-2437-2014.

[41] K. Sassen, Z. Wang, Classifying clouds around the globe with the cloudsat radar: 1-year of results, Geophysical Research Letters 35 (4) (2008). doi:10.1029/2007GL032591.

[42] D. K. Hall, G. A. Riggs, V. V. Salomonson, Development of methods for mapping global snow cover using moderate resolution imaging spectroradiometer data, Remote Sensing of Environment 54 (2) (1995) 127–140. doi:10.1016/0034-4257(95)00137-P.

Highlights

- An index is formulated from spectral absorption and angular scattering properties of clouds, which provides robust separation between water, ice, and mixed-phase clouds for a range of cloud optical and microphysical properties.

- As the ice fraction in the mixed-phase clouds exceeds 80%, phase discrimination between mixed-phase and ice clouds in the NIR wavelengths becomes increasingly challenging.

Author Statement

Manuscript Number: JQSRT-D-25-00277

TITLE: Sensitivity of Near-Infrared Bands to Cloud Phase: An Assessment Using Dual-View Satellite Measurements

Kameswara Sarma Vinjamuri: Conceptualization, Methodology, Software, Formal analysis, Visualization, Writing - Original Draft

Marco Vountas: Conceptualization, Supervision, Writing-Review & Editing

Vladimir Rozanov: Software, Writing-Review & Editing

Luca Lelli: Writing-Review & Editing

Hartmut Boesch: Supervision, Writing-Review & Editing

John P. Burrows: Supervision, Writing-Review & Editing

Declaration of interests

☒ The authors declare that they have no known competing financial interests or personal relationships that could have appeared to influence the work reported in this paper.

☐ The authors declare the following financial interests/personal relationships which may be considered as potential competing interests: